CHAPTER 2

Methodology and Characterization Tools

2.1 Introduction

One of the most important prerequisites for studying novel phenomena in topological systems is to manufacture materials in high-quality single crystalline form. Grain boundary effects play a key role in polycrystalline samples, smearing the delicate characteristics. Furthermore, the surface and bulk electronic states in topological insulators and semimetals exhibit different characteristics. The surface and bulk effects cannot be distinguished in polycrystalline samples due to the vast number of grains that are randomly oriented. The purest state of any chemical is a single crystal, which has extremely long-range atomic ordering. Additionally, well-defined crystallographic axes also allow researchers to study directionally dependent physical properties in both real and momentum space. In disorder-free materials, the charge carriers' mean free path is extremely long enable one to study quantum oscillations at low temperature and high magnetic field conditions. This provides opportunity to analyze the Fermi surface precisely. We used two approaches for the growth of single crystals- one is modified Bridgeman technique and another one is chemical vapour transport. The high purity elements (99.9% or above) were purchased from well-known commercials. The single crystal technology is the mother of all the recent technologies and modern sciences and useful in semiconductors, solar photovoltaics, turbine blades, helicopter blades and many more.

2.1.1 Modified Bridgeman Technique

The congruent melting method was used to grow $Bi_{0.95}Sb_{0.95}Dy_{0.1}Te_3$ sample (5% Dy in $BiSbTe_3$). High-purity elements (99.99% pure, Alfa Aesar/ Sigma Aldrich) were combined in a stoichiometric ratio in a quartz tube and vacuum sealed at 10-6 Torr. The sealed quartz tube was then placed into a furnace, steadily heated to 950 °C, and held there for 24 hours. The furnace was then cooled at a rate of 5 °C/h from 950 °C to 550 °C before being kept at 550 °C for another 72 hours for annealing. This annealing process was required to obtain

pure crystals. Finally, the furnace was progressively cooled to room temperature (60 °/ h). The image of cleaved single crystal sample is shown in Figure 2.1(a).

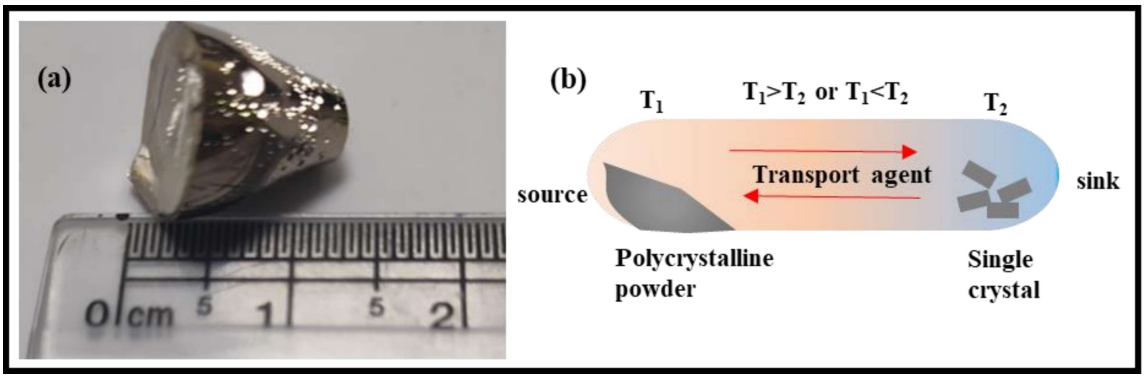

Figure 2.1: (a) Photograph of cleaved crystal sample, (b) schematic of CVT technique.

2.1.2 Chemical Vapour Transport Technique

The Chemical Vapor Transport (CVT) possess heterogeneous reactions in which a condensed phase lacks sufficient pressure for its volatilization, but can be volatilized in the presence of a gaseous reactant, also called transport agent and deposits elsewhere usually in the form of crystals. The successful single crystal growth occurs when temperature gradient is created. The polycrystalline material is transferred from the high temperature end (source) to the low temperature end (sink) as single crystals by an endothermic transport agent. Several parameters, such as the temperature gradient, rate of mass transfer, choice and mass of transport agent, and so on, must be optimised for successful growth of single crystal. We used iodine as transport agent. The polycrystalline powder and transport agent are enclosed in a quartz tube under vacuum (10^{-5} Torr) to avoid any possible impurity phase and preserve the vapour pressure. A two-zone tube furnace is used to achieve the required temperature gradient.

Single crystals of type 2 Weyl Semimetals were grown by the chemical vapor transport method in 3 steps. In the first step polycrystal of all the individual elements was synthesized by heating stoichiometric amounts at 800 °C for 24 h. This grown polycrystal was again

sealed in an evacuated quartz ampoule with iodine as a transport agent. The ampoule is put in the two-zone furnace with a temperature gradient 1050 °C (source) to 950 °C (sink) for two weeks and then quenched in ice-cold water. This fast-cooling process yields 1 T′-phase of the intended single crystal. The schematic of CVT method is shown in figure 2.1 (b).

2.2 Experimental characterization tools

2.2.1 X-Ray diffraction (XRD)

The most extensively used analytical technique for structural characterization and phase identification of crystalline materials is X-Ray diffraction. The samples used for measurements can be single crystal or polycrystal powders as well as thin films deposited on substrates. For a periodic atomic arrangement as in crystal lattice, each atom scatters the x-rays in all possible directions. The scattered beams interfere with each other either constructively or destructively. Constructive interference results in large enhancement of intensity and is observed at certain angles determined by the Bragg's law,

$$\boldsymbol{2d \sin \theta = n\lambda} \qquad \textbf{(2.1)}$$

Where n is an integer representing the order of diffraction, λ is the wavelength of X-ray used, d is the interplanar distance of atoms, and θ is the scattering angle or Bragg's angle. The schematic of X-ray diffraction from atomic planes are represented in Figure 2.2 (a).

For the powdered XRD, samples were measured by crushing and grinding the single crystals. A freshly cleaved rectangular piece of the sample was taken to do the single crystal XRD. To extract the space group symmetry and lattice parameters, the experimental data have been analyzed by Rietveld structural refinement using the FULLPROF software package. The intensity of diffracted X-ray is recorded as a function of the Bragg angle 2θ. The Rigaku-Miniflex II DESKTOP powder X-ray diffractometer, as shown in figure 2.2 (b), was used to record the intensity vs. 2θ data in the range 10°- 80° with a 0.02° gap. This

diffractometer has a monochromatic X-ray source with CuK_α radiation (λ=1.5418Å) at 30 kV and 15 mA.

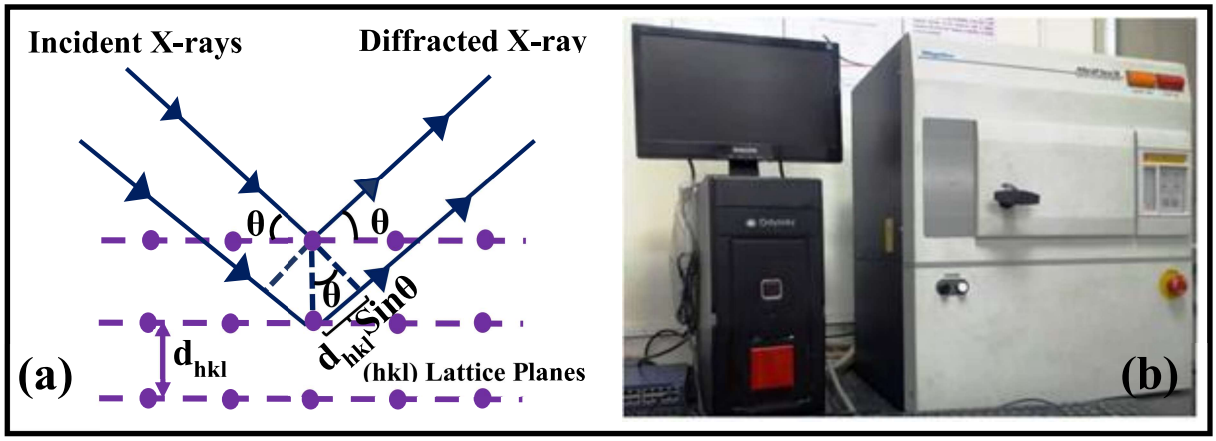

Figure 2.2: (a) Schematic of x-ray diffraction by crystallographic planes (b) Image of Rigaku Mini Flex II DESKTOP lab based XRD set up.

As we know for x-ray diffraction, Bragg's condition needs to be satisfied. There are two methods to satisfy the Bragg's condition. First, we can change the initial wavelength keeping the diffraction angle constant θ_{hkl}, it gives the energy dispersive x-ray diffraction (EDXRD). Secondly, we can keep the wavelength fixed but change the angle θ_{hkl}, it is known as angle dispersive x-ray diffraction (ADXRD). Both holds some pros and cons. EDXRD is fast and possess better signal to noise ratio, but the resolution is of the order of $\sim10^{-2}$, whereas, ADXRD is relatively slower process but the resolution is much better $\sim10^{-4}$. Generally, in laboratory for high pressure experiments, ADXRD is preferred because it provide better resolution. An ADXRD set up contains the x-ray source, sample mounting stage for DAC and a detector with computer-based reading set up. For a polycrystalline sample, all crystal orientations θ_{hkl} are possible with equal probability. So, x-ray radiation, scattered symmetrically about the primary x-ray beam. If Bragg's condition is satisfied diffraction rings are obtained. High pressure single crystal experiments are limited up to the low-pressure range due to experimental limitations of loading and sustaining the crystal at high pressure without breaking. Size of the x-ray beam should be sufficiently smaller

than the gasket hole size. If it is not the case then diffraction pattern of gasket may interfere with that of the sample. Diamond anvil cell is placed over the XY stage which can be moved to focus the x-ray beam on the sample. Diffracted beam which comes out of the backing plate is recorded on the detector. Incident photons charge the semiconductor pixels on detector. The image is first calibrated for detector distance, wavelength, beam centre position, polarization and orientation with the help of programs such as FIT2D. Integrated pattern was fitted with model structure and the difference between the experimental and model is minimized by least square method using available program such as GSAS.

For x-ray generation, either laboratory based rotating anode generator or synchrotron source is used. For high pressure experiments, sample size is very small (of the order of few micron), so total intensity of scattered light is low. Synchrotron sources are very intense (10^4-10^{10}) and provide diverge usage compared to the lab-based sources. Additionally, selection of various wavelengths ranging from 10 pm-100 pm are also possible in synchrotron sources. However, rotating anode source may only provide few fixed wavelengths such as Cu~1.5406 Å and Mo~0.7093 Å *etc*. Synchrotron radiation enable us to access large k-space/ θ angle, which is important for diffraction analysis. While scattering power of the crystal vary with λ^3, but larger wavelengths are easily absorbed by the materials. So, the synchrotron-based sources are preferred over any other sources. Along with the source, intensity, wavelength, efficiency of the detector plays a crucial role for high pressure experiment. For higher wavelength, efficiency of the detector increases.

2.3 Transport properties measurements

2.3.1 Electric resistivity (ρ_{xx})

Resistivity of the synthesized single crystal samples was recorded using Quantum Design Physical Property Measurement system (QD-PPMS) by adopting five-probe/four-probe method. When electrons travel through the crystal, they feel the resistance in their motion. To

move the electrons against this resistance a potential difference is needed to apply across the crystal. According to Ohm's law, if current I flow through the crystal that have resistance R, then voltage V will drop against this resistance through the crystal from equation V= IR. The quantity that characterizes the material is resistivity (ρ_{xx}). The resistivity of particular material depends on the synthesis process. The resistivity of a crystal is inversely proportional to the length l between two voltage probes and proportional to the cross-section area A. Mathematically, it is expressed as

$$\boldsymbol{\rho_{xx} = \frac{RA}{l}} \quad \textbf{(2.2)}$$

The density and mobility can be obtained using Hall measured and we can calculate thosde parameters using following equations-

$$\boldsymbol{R_H = \frac{1}{ne}} \quad \textbf{(2.3)}$$

$$\boldsymbol{\mu = \frac{R_H}{\rho_{xx}}} \quad \textbf{(2.4)}$$

The resistivity measurements were carried out on a uniform rectangular single crystal sample by employing a conventional four-probe/five -robe technique between 2 K and 300 K with (MR) and without (ordinary resistivity) applying external magnetic field B normal to the surface of sample as shown in figure 2.3 (a). The Hall measurement configuration is shown in Figure 2.3 (b). The current (I) was flown between two outer terminals, whereas the voltage (V) was measured between two inner contacts. The value of the resistance (R = V/I) is recorded within the temperature range 2-300 K in with 9 T superconducting magnet. The image of the PPMS system is shown in Figure 2.4. The electrical resistivity ρ is also measured with van der Pauw (vdP) method (UGC-DAE Kalpakkam) using the following equation-

$$\boldsymbol{\rho = \frac{\pi d}{\ln 2}\left(\frac{R_1 + R_1}{2}\right) f} \quad \textbf{(2.5)}$$

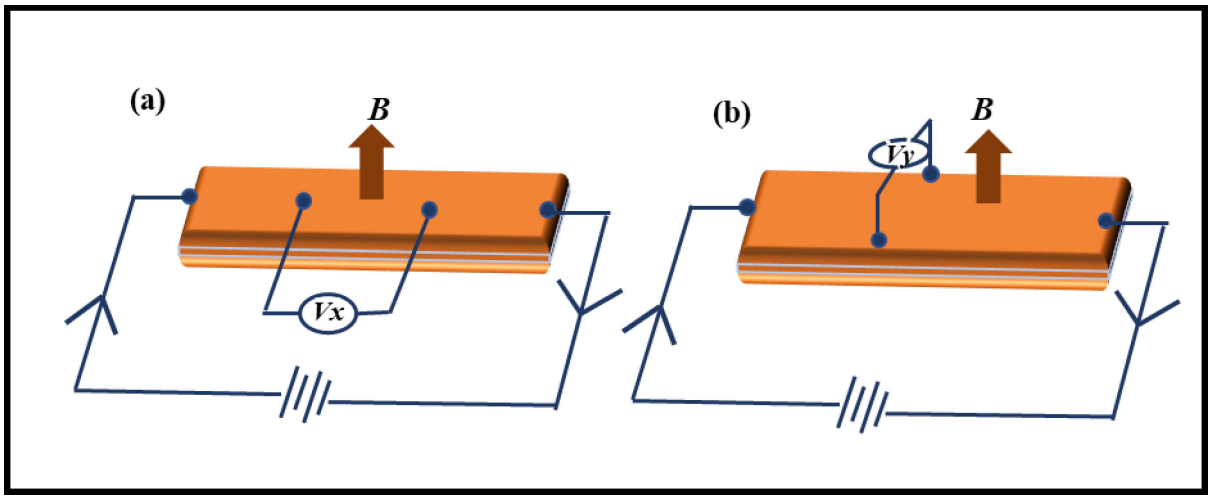

Figure 2.3: Schematic for (a) longitudinal resistivity measurements using four-probe geometry and (b) Hall resistivity measurements using four-probe geometry. The magnetic field is applied orthogonally to the applied electric current (I).

In Figure 2.5, we have illustrated the steps followed to measure the longitudinal resistivity (a and b), and the Hall resistivity (c and d) using this vdP method.

The Figure 2.5 (upper panel) illustrates that resistance R1 is obtained applying a current I between the leads I_+ and I_- and then measuring the voltage across the contacts V_+ and V_- (V_{xx}), while R2 is obtained altering the current terminal, and then R3 is measured changing the voltage terminal and finally R4 is obtained altering the current terminals. In equation (2.5), d is the sample thickness and f is a geometric factor dependent of the R_2/R_1 ratio. No significant difference between V_{xx} and V_{yy} slopes were observed, so f≈ 1 was obtained using numeric calculations and no geometric corrections are required. The steps were taken to obtain $V_{xy}^{'}$ and $V_{xy}^{''2}$ values, respectively. A magnetic field (B) is required and its intensity has to be sufficient for the transversal voltage (V_H) induction. So, we can write:

$$V_H = \frac{V_{xy}^{'} - V_{xy}^{''2}}{2} \qquad (2.6)$$

And the Hall coefficient is –

$$R_H = \frac{V_H}{BI} d \qquad (2.7)$$

vdP method is used for measuring resistivity and Hall coefficient of samples of any shape with uniform thickness. The current and voltage leads must be measured and averaged accurately for numerous unique permutations in order to use this technique with the optimal precision. The Hall measurements are very accurate using this configuration. VdP method eliminates 3 distinct sources of systematic measurements errors:

- Effect of the contact resistance
- Thermal EMF in wires, cables and connectors
- Effects of sample geometry and position of the contacts

This is achieved by using 4-terminal resistance measurement in a flat sample with uniform thickness and various permutation of contacts for supplying current and reading voltage.

Figure 2.4 The Physical property measurement system (PPMS) set up at UGC-DAE, Kalapakkam node.

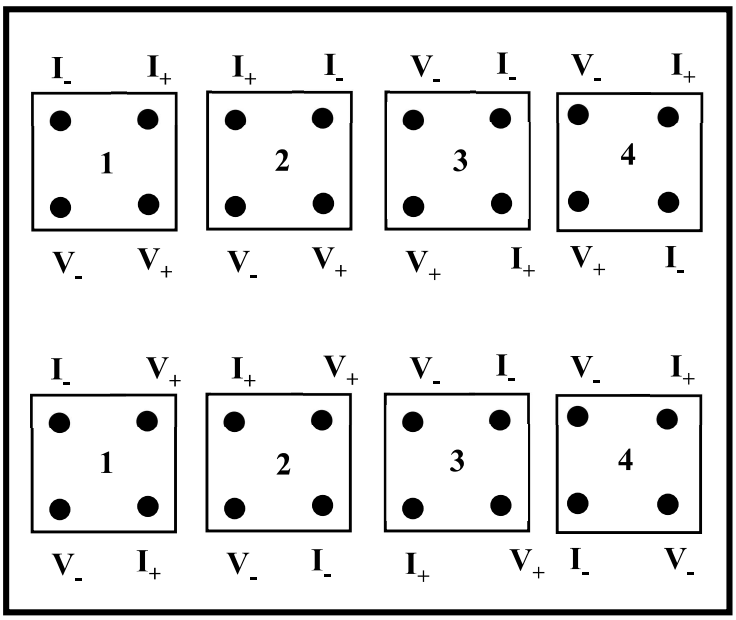

Figure 2.5 Van der Pauw contact configuration for measuring the resistivity: **upper panel-** longitudinal resistivity (MR), **lower panel-** transverse resistivity (Hall).

2.4 Magnetic Measurements

2.4.1 DC magnetization and AC susceptibility

The dc magnetization measurements were carried out in a superconducting quantum interference device (SQUID) - vibrating sample magnetometer (VSM) (MPMS3, Quantum Design). This instrument operates in the temperature range 1.8-400 31 K with maximum sweep rate 50 K/min and under a magnetic field up to 7 T, which can be varied at a rate up to 700 Oe/sec. The minimum magnetic moment that can be accurately measured is as small as 5×10−8 emu. In Figure 2.6, we have shown a simplified schematic of the experimental set-up. The superconducting detection coils function as a second order gradiometer, where the counter wound outer loops ensure that the set of coils are non-responsive to uniform magnetic fields or linear magnetic field gradients. The detection coils produce a current due to local magnetic field disturbances generated by the vibrating sample. If the sample dimensions are much smaller than those of the detection coils, then the current is a function of the position of the sample. This current in the detection coils is inductively coupled to

the SQUID, which serves as an ultra-sensitive current to voltage converter. The basic function of SQUID is governed by two phenomena, flux quantization in a superconducting ring and Josephson effect. The Josephson effect describes the current flow across a Josephson junction, i.e., two weakly coupled superconductors separated by a thin insulating barrier. SQUID feedback nulls the current in the detection coils so no current actually flows in them, and the feedback current yields the actual SQUID voltage that gives the sample magnetization value.

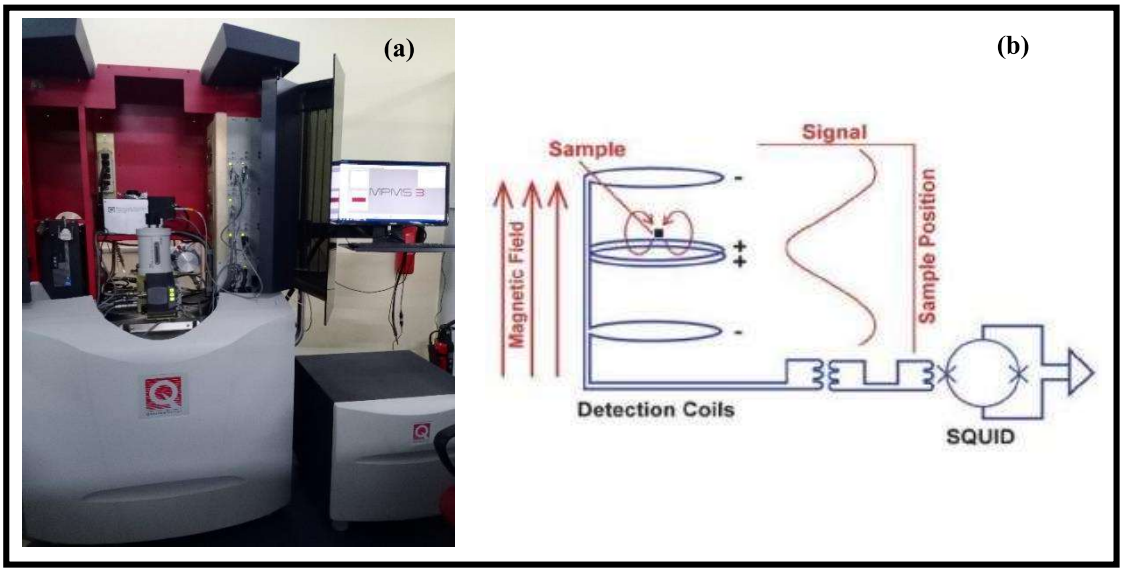

Figure 2.6 (a) Image of Quantum Design MPMS3 of CIFC, IIT (BHU), (b) Schematic diagram of SQUID-VSM detection system [108].

This system provides three possible mode of magnetization measurements: (i) DC scan mode (ii) AC susceptibility mode and (iii) VSM (vibrating sample mode). We have used vibrating sample mode in our investigation. The VSM vibrates the sample at a frequency ω about the centre of the detection coils. The signal received by the detection coil varies as a function of the sample position (z). Then, at time t, the generated signal by the SQUID is

$$V(t) = AB^2 \sin^2(\omega t) \qquad (2.8)$$

as V (z) = Az^2 for small vibration amplitudes and z(t) = B sin(ωt). A is a scaling factor relating to the magnetic moment of the sample, whereas B is the amplitude of sample vibration. As $\sin^2(\omega t) = 1/2[1-\cos(2\omega t)]$, a lock-in amplifier is used to 32 Figure 2.6 shows simplified schematic of the SQUID-VSM detection system isolate the signal occurring at frequency 2ω, which is generated exclusively by the sample, provided the vibration frequency is selected properly. This is achieved by multiplying the measured signal with a phase-corrected reference signal at 2ω and then extracting the dc component of the result. The dc component is proportional to the 2ω component of the measured signal. This technique precisely isolates the sample signal from other noise sources, including drifting SQUID signal and mechanical noise sources synchronized to the sample vibration. The lock-in amplification of the SQUID signal is performed by digital electronics in the control module.

2.5 Raman spectroscopy

In 1928, C. V. Raman discovered the Raman effect, which describes the inelastic scattering of light by a substance. When a material is illuminated by light, majority of the photons scatter elastically, called Rayleigh scattering and in this case, the scattered frequency remains same with the initial one. On the other hand, very small fraction scatter inelastically called Raman scattering in which the final frequency is greater/smaller than the incident one. These inelastically scattered photons carry the energy of the characteristic molecular vibrations in the sample, resulting the shift of their frequency. The theory of the microscopic origin for Raman effect can be constructed as follows [56]. An incident photon of angular frequency ω_i can interact with a material by creating or destroying one or more lattice vibration quanta (phonon). In this process, the energy ~ω lost or gained by the lattice is compensated by the increase (anti-Stokes component) or decrease (Stokes component) in the frequency (ω_s) of the scattered photon ($\omega_s = \omega_i \pm \omega$). If we consider the first-order

Raman effect, i.e., where a single phonon is created or destroyed in the scattering process. Figure 2.7(a) illustrates the process for generating the Stokes component. Figure 2.7 (b) represent different Raman vibration modes.

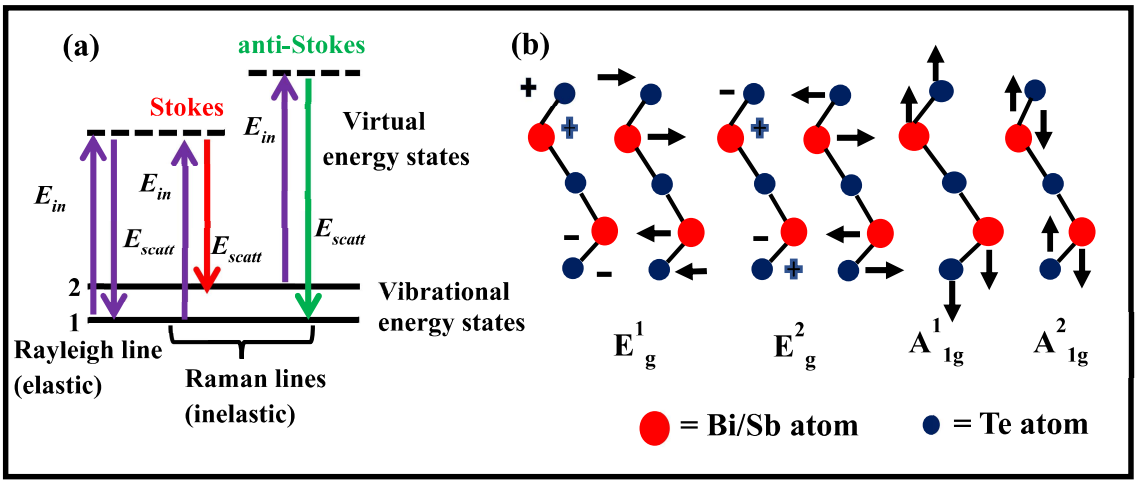

Figure 2.7 (a) Energy-level diagram presenting the states involved in Raman scattering process, (b) Schematic diagram of Raman active vibrational modes.

Note that three steps are involved, a photon (ωi) is absorbed, an optic phonon (ω) is created and a photon (ωs) is emitted. 34 Figure 2.7: (a) Elementary Raman scattering process. Reproduced from Ref. [56]. (b) Energy-level diagram showing the states involved in Raman scattering process. At the start of the scattering process, the scattering material is generally in its electronic ground state with filled valance bands and empty conduction bands. It again returns to its ground state at the end of the scattering event. The virtual intermediate states involve the excitation of electron-hole pairs. Depending on whether the incident photons interact with a molecule in its vibrational ground state or excited state, the scattering signals appear either at the low energy or high energy side, respectively. As shown in Figure 2.7(b), the Stokes scattering excites the scatterer to an upper energy state. On the other hand, anti-Stokes emission occurs only if the scatterer, which is already at an upper energy state, decays to a lower state. The Stokes and anti-Stokes Raman modes reside

symmetrically around the Rayleigh line as they are generated by same upper and lower energy states. However, anti-Stokes lines have lower intensity compared to the Stokes lines, because the number of molecules in an excited vibrational state is very small. Nowadays, Raman spectroscopy has become a popular, non-destructive and powerful technique to investigate the lattice dynamics and structural symmetries of a system.

Temperature dependent Raman study was executed by Horiba LabRam HR evolution spectrometer. The sample was irradiated with 633 nm He-Ne laser. The sample was cooled from 300 to 100 K by liquid nitrogen when taking Raman measurements at different temperatures.

2.6 High pressure measurement techniques

High pressure is an external parameter used to create extreme environment for a material, where new quantum phenomena can emerge. Instead of the complex chemical doping, this technique provides us an effective and clean way to tune the crystal structure as well as chemical potential of a material. We put the sample under pressure up to 35 GPa using a diamond-anvil-cell (DAC). Using diamonds to generate high pressure has certain advantages [57]. In addition to Figure 2.8: Schematic of a diamond-anvil-cell used for generating high pressure. Reproduced from Ref. [58]. be the hardest material known to us, diamond is transparent to infrared, visible, ultraviolet (< 5 eV), and x ray (> 10 keV) radiations, making it suitable for optical spectroscopy and x-ray diffraction experiments. Moreover, it is chemically inert and compatible to electrical and magnetic transport measurements. In Figure 2.8, the schematic of a DAC is shown. Two opposing diamond anvils with small 36 culets point to each other such that the tips of the anvils generate pressure on the sample, floating in a pressure transmitting medium. We used either silicone oil or Ne gas as the transmitting medium, which ensures good hydrostatic condition at the sample space. Stainless steel or rhenium gaskets were used. The pressure was calibrated

using either fluorescence of ruby or equation of state of gold and platinum, which were loaded in the DAC along with the sample.

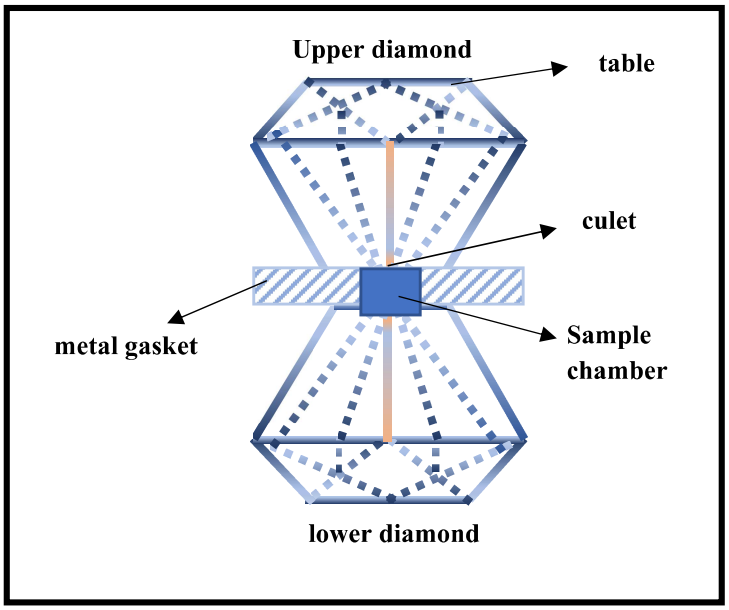

Figure 2.8 Schematic of a diamond-anvil-cell (DAC) used for generating high pressure.

High pressure Raman set up includes the diamond anvil cell which contain the pressurized sample. Excitation laser light is focused by an objective lens on the sample in gasket hole. Sample in DAC is kept in at one of the focal points of the coaxial lense system. Scattered light is collected by the same objective and directed toward the spectrograph by a combination of lenses. A holographic edge filter is used to eliminate the Rayleigh wavelength. Rest of the collected light is dispersed by the gratings and recorded by the CCD detector. Collected spectra is shown on the computer screen. Photograph of Raman system used for studies included in Fig. A new confocal Raman scattering for high pressure experiments is installed in the laboratory and details are given.

High pressure angle dispersive powder x-ray diffraction experiments (ADXRD) were carried out in a modified Mao Bell diamond anvil cell (DAC) at the BL-11 beamline at

INDUS2, Indore, India using a 0.7842Å wavelength. Single crystal samples were finely powdered and were loaded in the sample chamber of a pre-indented tungsten gasket of the thickness ~50 μm and hole diameter ~120 μm. Daphne oil was used as pressure transmitting medium (PTM) for these experiments as in many of these samples methanol:ethanol (4:1) mixture was found to be reacting with the sample. Copper was loaded along with the sample and the pressure was monitored using its equation of state. The diffraction data was collected with the help of a MAR345 imaging plate detector. The sample to detector distance was calibrated with the help of a standard NIST sample LaB_6[109]. The two-dimensional image was converted to intensity verses angle data with the help of the FIT2D software and further Rietveld refinement analysis was done by GSAS.

High pressure Raman scattering experiments were carried out using a Diode Pumped Solid State (DPSS) laser of 532 nm wavelength. Pressure was monitored using R-lines of ruby fluorescence and calculated for quasi-hydrostatic conditions. All measurements were recorded in the backscattering geometry using a triple stage spectrograph (Jobin Yvoun T64000) in subtractive mode with resolution ~ 2cm^{-1} equipped with a Peltier cooled detector operated in the triple spectrograph mode.

2.7 Fundamentals of ARPES

The angle resolved photoemission spectroscopy (ARPES) was initially identified by Hertz in 1887 based on the photoelectric effect, Einstein later elucidated the microscopic mechanism of this phenomenon in 1905, when he proposed the idea of a photon, quantum of light. A sample is positioned close to an electron analyzer in an ultrahigh vacuum during the ARPES measurement. When light strikes on the surface of a material, the electrons inside the material absorb photons; if the energy of the photons is higher than the material's work function, the electrons can escape from the surface. These photo-emitted electrons,

called photoelectrons, are then collected and analysed with respect to their kinetic energy and emission angle by a spectrometer. The energy and momentum of the electrons inside the sample are directly connected to those of the photoelectrons by the conservation of energy and momentum parallel to the sample surface. Under the emission angles θ and φ defined in Fig. 1a, the following relationships follows-

$$\boldsymbol{E_{Kin} = h\nu - \phi - E_B} \quad \textbf{(2.9)}$$

E_{Kin} is the kinetic energy (K.E) of a photoelectron; hν is the photon energy; E_B is the binding energy of the electron inside the sample; and ϕ is the work function of the material. This is the energy required for an electron at Fermi energy E_F to escape to the vacuum level (E_{vac}) where $\Phi = E_{vac} - E_F$.

$$\hbar \boldsymbol{k}_{\parallel}^{f} = \hbar \boldsymbol{k}_{\parallel}^{i} \sqrt{\boldsymbol{2mE_{Kin}}} (\boldsymbol{\sin\theta\cos\phi k_x + \sin\theta\sin\phi k_y}) \quad \textbf{(2.10)}$$

where $\hbar k_{\parallel}^{f}$ and $\hbar k_{\parallel}^{i}$ are the parallel components (with respect to the sample surface) of the momenta of the photoelectron and the initial electron, respectively; θ and φ are the emission angles of the photoelectron; ħ is the reduced Planck's constant; and m is the electron rest mass. The above conservation laws are when the relaxation time of the electron–hole pairs is much longer than the escape time of the photoelectrons and the momentum of the photons is much smaller than the momentum of the photoelectrons.

The momentum perpendicular to the surface, is not conserved because of broken translational symmetry in this direction $\hbar k_{\perp}^{f} \neq \hbar k_{\perp}^{i}$ where $\hbar k_{\perp}^{f}$ and $\hbar k_{\perp}^{i}$ the perpendicular components of the momenta of the photoelectron and initial electron, respectively. This $\hbar k_{\perp}^{i}$ can be extracted as-

$$\hbar \boldsymbol{k}_{\perp}^{\boldsymbol{i}} = \sqrt{\boldsymbol{2m(E_{Kin}\cos^2\theta + V_0)}} / \hbar \quad \textbf{(2.11)}$$

V_0 is a constant called the inner potential and determined from photon-energy-dependent measurements by fitting the experimental periodicity along the $k_{\perp}^{i}$ direction. Once V_0 is

found, $k_{\perp}^{i}$ is easily determined. Thus, to investigate the electronic structure in the 3D Brillouin zone, photon-energy-dependent ARPES measurements are an effective route to study the Topological materials in depth. A schematic representation of ARPES is depicted in Figure 2.9(a). Figure 2.9 (b) represents energy band dispersion of topological insulators Bi_2Te_3, Sb_2Te_3, Bi_2Se_3 and for the band insulator Sb_2Se_3.

ARPES is a very surface-sensitive technique, and significant portion of the overall signal will be used to observe the sample's topmost surface layer. This surface sensitivity is helpful in investigating surface states, such as those in topological insulators and Weyl semimetals. but necessitates the use of flat surfaces that are atomically clean and well-ordered for ARPES investigations. Single crystals are often cleaved in situ and measured in ultrahigh vacuum chambers (~10^{-11}Torr) to get a clean surface and prevent surface contamination. There are many 3D materials which are not easily cleavable thus limits the measurements of ARPES.

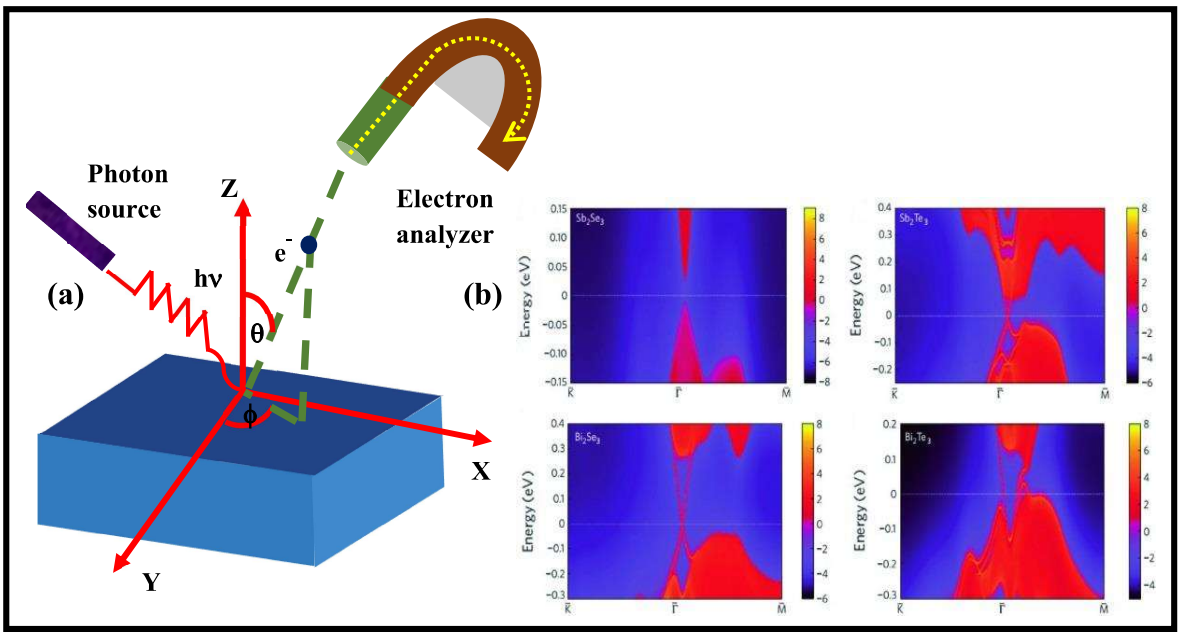

Figure 2.9 Schematic of ARPES measurements, **(b)** Energy and momentum dependence of the local density of states for (a)Sb_2Se_3, Sb_2Te_3, Bi_2Se_3, and Bi2Te3 on the [111] surface. The red and blue regions indicate bulk energy bands and bulk band gaps, respectively. The

red lines, dispersing in the bulk gap around the Γ point, are the surface states. Reproduced from Ref. [25].

2.8 Theoretical density functional theory (DFT) calculation

The theoretical calculations were performed using VASP (Vienna ab initio simulation package)[110] to probe the electronic properties of various materials. The simulations use the GGA (generalized gradient approximation) of PBE (Perdew-Burke-Ernzerhof) exchange-correlation functional. A plane wave basis with a cutoff of 400 eV was used and spin orbit coupling (SOC) was included in all calculations. The Gaussian smearing method along with a smearing width equal to 0.10 eV was chosen for Brillouin zone integration. We followed the energy convergence limit up to 1×10^{-5} eV for all sets of calculations. To simulate the 5% doped compounds, a 2×2×1 supercell with 1 atom out of total 60 atoms is constructed for the calculation[111]. Experimental lattice parameters and wycoff positions were used to perform the calculation. A K-mesh of 8×8×1 was generated for the self-consistent field (SCF) run followed by band structure and DOS calculations.